Electronic Supplementary Material (ESI) for Physical Chemistry Chemical Physics.

Supplementary Information

Bringing light into the dark triplet space of molecular systems

Jing Ge,[a] Qun Zhang,*[a,b,c] Jun Jiang,*[a,b,c] Zhigang Geng,[b] Shenlong Jiang,[b] Kaili Fan,[a] Zhenkun Guo,[a] Jiahua Hu,[a] Zongwei Chen,[a] Yang Chen,[a,b,c] Xiaoping Wang[b,c] and Yi Luo*[a,b,c,d]

[a] *Department of Chemical Physics, School of Chemistry and Materials Science, University of Science and Technology of China, Hefei, Anhui 230026, China.*
[b] *Hefei National Laboratory for Physical Sciences at the Microscale, University of Science and Technology of China, Hefei, Anhui 230026, China.*
[c] *Synergetic Innovation Center of Quantum Information and Quantum Physics, University of Science and Technology of China, Hefei, Anhui 230026, China.*
[d] *Department of Theoretical Chemistry, School of Biotechnology, Royal Institute of Technology, AlbaNova, S-106 91 Stockholm, Sweden.*

*Corresponding Authors:
qunzh@ustc.edu.cn (Q.Z.); jiangj1@ustc.edu.cn (J.J.); yiluo@ustc.edu.cn (Y.L.).

This PDF includes

- **Details of the femtosecond pump−probe experiments**
- **Details of the first-principles calculations**
- **A typical case study using conventional pump−probe scheme (Fig. S1)**
- **ME ($T_3 \rightarrow T_2$) kinetics fitting results (Fig. S2)**
- **More details of WLC filtering tests (Fig. S3)**
- **Another case study using a combination of WLC and 400-nm (instead of 580-nm) lasers and relevant discussions (Fig. S4)**
- **Crude modeling and preliminary simulations on ME and SET (Fig. S5)**

➢ Details of the femtosecond pump–probe experiments

The fs pump–probe experiments (in both conventional and TRPP regimes) were performed on a modified ExciPro system (CDP) in combination with an ultrafast amplified laser system (Coherent). All the measurements were performed under ambient conditions. The schematic of the optical layout is shown in Fig. 1 of Article.

The pump pulses (centre wavelengths mainly in the visible: 400–700 nm for this study; pulse energy ~10 μJ at the sample cell) were delivered by an optical parametric amplifier (TOPAS-800-fs), which was excited by a Ti:sapphire regenerative amplifier (Legend Elite-1K-HE; centre wavelength 800 nm, pulse duration 25 fs, pulse energy 3 mJ) seeded with a mode-locked Ti:sapphire laser system (Micra 5) and pumped with a 1-kHz Nd:YLF laser (Evolution 30). The probe pulses (~1 μJ/pulse at the sample cell) were provided by a stable white-light continuum (WLC) (340–1550 nm; 0.80–3.65 eV) that was generated by focusing the 800-nm beam (split from the regenerative amplifier by a portion of 10%) in a rotating CaF_2 crystal (for 340–1100 nm) and a stationary sapphire crystal (for 1000–1550 nm). The linear chirp of the WLC spectrum was compensated with the aid of the cross-phase modulation signals recorded on a liquid hexane sample using an ExiPro 2.6 software. The WLC pulse was free of pre-pulsing and after-pulsing, as verified by our routine pulse characterizations. The pump and probe beams were collinearly polarized. The instrument response function was determined to be ~100 fs by cross-correlating the pump and probe pulses at the sample cell.

Precise spatial overlap of the pump and probe beams (diameters ~800 and 300 μm, respectively) at the centre of the 1.2-mm-thick sample cell (quartz) was attained by optimizing the transient signals with the aid of a laser beam analyzer (BG-USB-SP620, Ophir-Spiricon). The delay times between the pump and probe pulses were varied by a motorized optical delay line (minimum step 1.56 fs; maximum delay 2.0 ns). The delay time zero was determined by cross-correlating the pump and probe pulses at the sample cell *in situ* and also carefully cross-checked with other chemical samples such as the DCM and LDS698 dyes.

A chopper operating at 500 Hz was used to modulate the pump pulses such that the transient spectra with and without the pump pulses can be recorded alternately. The WLC probe beam was first split into two tiny portions to synchronize the chopper and monitor the stability of the probe pulses using two separate photodiode detectors, and then separated into two parts (intensity ratio ~70:30), with the 70% part focused on the sample cell and overlapped with the pump beam yielding a transmitted probe signal, while the 30% part focused onto another place of the sample cell to serve as a reference signal for achieving a best signal-to-noise ratio.

The sample cell containing an aqueous solution of MG (1.5 mM) was mounted on a rapidly rotating stage (5000 rpm) to ensure that the photoexcited volume of the sample was kept fresh during the course of the measurements. The temporal and spectral profiles of the pump-induced/modulated differential transmission of the WLC probing light were visualized by a 1024-pixel imaging spectrometer (CDP2022i) and further processed by the ExiPro 2.6 software.

➢ Details of the first-principles calculations

Molecular models were built for the MG molecule. The optimized geometry, electronic structures, and vibronic profiles (normal modes) were simulated with the density function theory (DFT) using the Gaussian 09 package at the B3LYP/6-31++G** level [Ref. S1]. The water solvent effect was considered with the polarizable continuum model. Time-dependent DFT calculations at the same level [Ref. S2] were conducted to find out the excited states (for both singlets and triplets) and to generate the single-photon absorption spectrum. The linear coupling model was used to compute the Franck–Condon distributions with the program we developed in 2005 [Ref. S3]. Based on the calculated excitation levels (ε_i) and probabilities s_i at the DFT level, we have employed the Lorentz broadening function to describe the distribution profile *S(E)* of the absorption and ultrafast spectra observed in experiments, where $S(E)=\sum_{i=1,N}\frac{s_i\Gamma}{(E-\varepsilon_i)^2+\Gamma^2}$. Here Γ can be determined by $\Gamma=\sqrt{(k_{\mathrm{B}}T)^2+\sum_{j=1,m}(\hbar\varpi_j)^2}$, where $k_{\mathrm{B}}T=0.026\,\mathrm{eV}$ at room temperature and ϖ_j represents the frequency of the possible vibrational mode involving excited molecules and solution bath. Unfortunately, it is very expensive to calculate directly the interactions and vibrations between transition dipoles and the constantly fluctuating solvent molecules. Therefore, here we follow the standard procedure of many works that employs an empirical broadening factor with $\Gamma = 0.3$ eV [Ref. S4].

The environmental effect can often affect the photo-response of molecules. In our experiment, the MG molecule is working in the aqueous solution with Cl^- ion. It is known that polar molecules almost always establish hydrogen bonding with solvent molecules, which could easily change the transition diploes and shift the excitation/emission photon energies for molecules. Meanwhile, the Cl^- ions form contacts with the N^+ in the MG molecules, driven by the electrostatic interactions. This means that the MG molecule is actually not working under neutral condition, and an electron should have been transferred from the MG to a Cl atom. To illustrate the effects of specific interactions, we have examined four different molecular models including (*i*) the neutral MG molecule attached to a Cl^- ion, (*ii*) model (*i*) attached to two water molecules through the N–H hydrogen bond, (*iii*) the MG molecule with one positive charge (i.e., one electron donated to solvent), and (*iv*) model (*iii*) attached to two water molecules through the N–H hydrogen bond. As expected, the computed absorption spectrum based on model (*iv*), which takes into account both hydrogen bonding and charge distribution due to ions interaction, provided the best agreement with the experimental observation. Therefore, the relevant discussions on MG's singlet and triplet excited states as well as the population dynamics involved are all based on model (*iv*).

References

[S1] M. J. Frisch, *et al*. *Gaussian 09 Revision A.1*, Gaussian Inc., Wallingford CT, 2009.

[S2] M. Caricato, *et al*. *J. Chem. Phys.*, 2006, **124**, 124520.

[S3] Y. H. Wang, M. Halik, C. K. Wang, S. R. Marder and Y. Luo, *J. Chem. Phys.*, 2005, **123**, 194311.

[S4] S. Mukamel, *Principles of Nonlinear Optical Spectroscopy*, Oxford University Press, New York, 1995.

➢ Supplementary Figures S1–S5

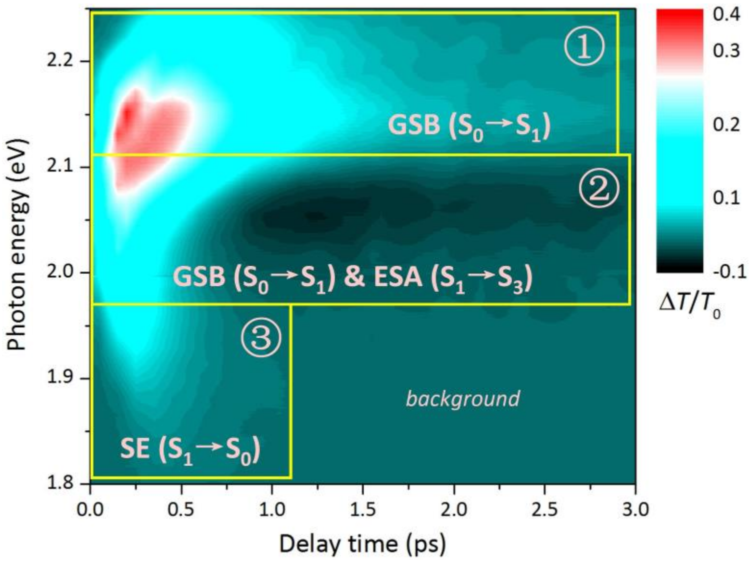

Fig. S1 Singlet dynamics in MG: A conventional fs pump–probe study. In this representative case study, a combination of 580-nm pump and delayed WLC probe (1.8–2.25 eV; 550–690 nm) was used. With the aid of the known state energetics in the singlet space (Fig. 3 of Article), one can readily assign the observed transients to the strongly allowed transitions of ① GSB ($S_0 \rightarrow S_1$) alone, ② coexisting GSB ($S_0 \rightarrow S_1$) and ESA ($S_1 \rightarrow S_3$), and ③ SE ($S_1 \rightarrow S_0$) alone, where GSB, ESA, and SE denote ground-state bleach, excited-state absorption, and stimulated emission, respectively. MG is the acronym for the molecule of malachite green, whose molecular structure is given in the inset of Fig. 2 of Article.

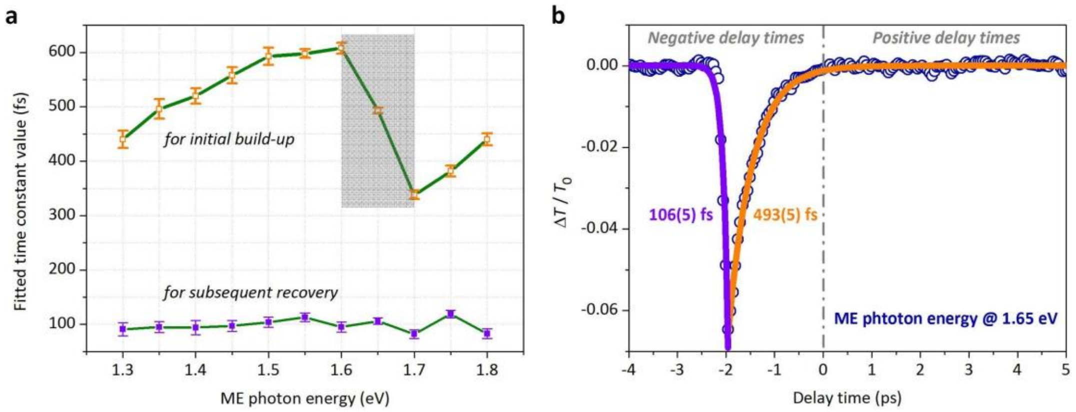

Fig. S2 Fitting results for the ME ($T_3 \rightarrow T_2$) kinetics observed in MG under the fs-TRPP regime. (a) The data derived from the mono-exponential fitting for both the initial build-up and the subsequent recovery. (b) Representative curve fitting for the kinetic trace taken at the ME photon energy of 1.65 eV. ME and MG are the acronyms for modulated emission and malachite green, respectively.

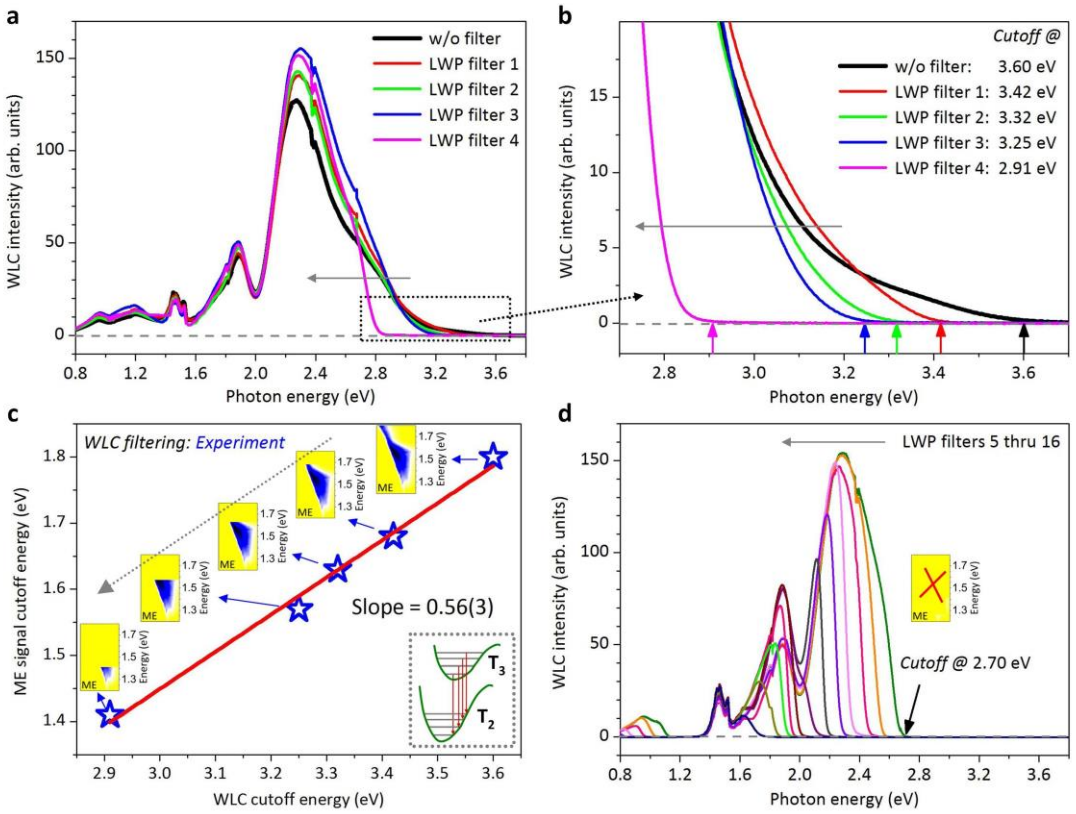

Fig. S3 WLC filtering in ME: Experiment. (a) The use of the four LWP filters (colored lines) to chop the high-frequency components of the original, broad WLC spectrum (thick, black line) makes the high-photon-energy portions of the observed ME transients (see Fig. 5a of Article) systematically disappear [refer to (c)]. (b) An expanded view of the region marked by a dotted box in (a). (c) A clear linear dependence of the ME cutoff energies (insets in chains) vs. the corresponding WLC cutoff energies [given in (b)]. The lower-corner inset depicts the potential shift between T_3 and T_2 caused by Franck–Condon distributions. (d) The use of this set of LWP filters (all with cutoffs below 2.7 eV) completely diminishes the observed ME pattern (inset). Note that all the recorded WLC intensities have not been calibrated against the spectral response of the imaging spectrometer. WLC, LWP, and ME are the acronyms for white-light continuum, long-wave pass, and modulated emission, respectively.

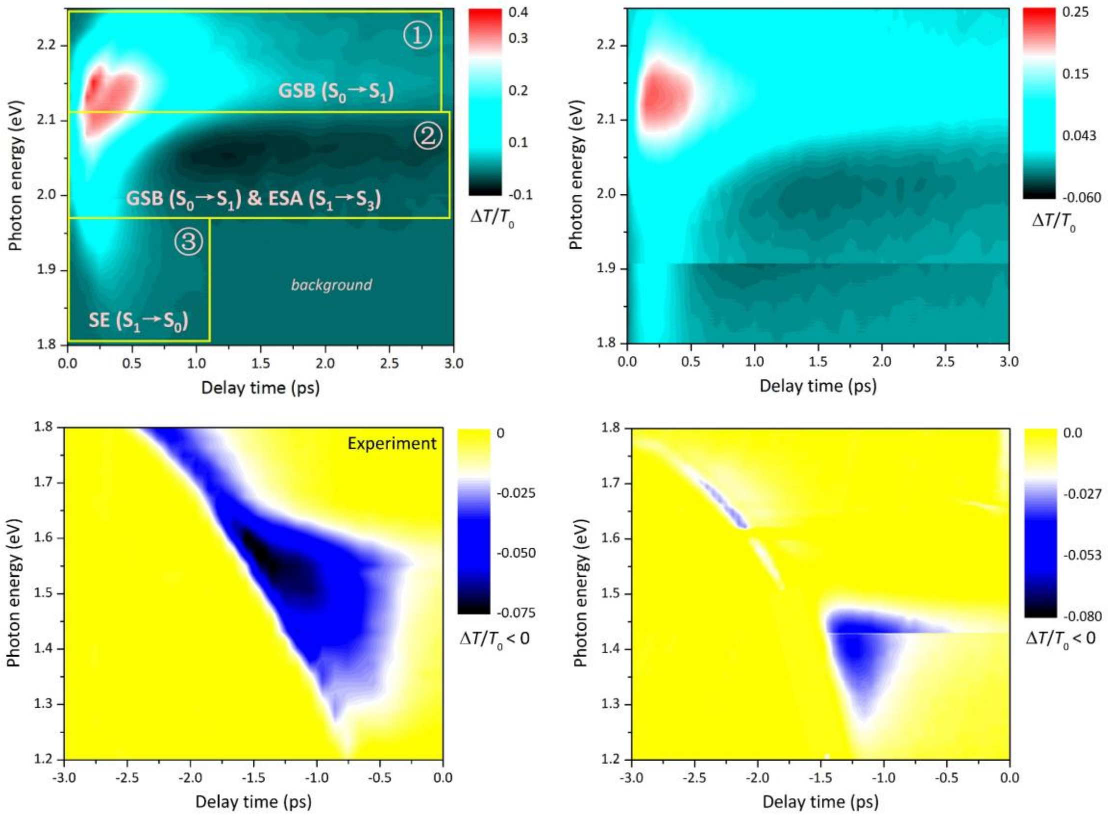

Fig. S4 Another case study using a combination of WLC and 400-nm (instead of 580-nm) lasers. **Upper left panel:** The 580-nm pumping case (adapted from Fig. S1). **Upper right panel:** The 400-nm pumping case. The same WLC probe was used. **Relevant discussions:** In the conventional pump–probe scheme (using the “quasi-monochromatic” 400-nm pulse to excite S_2), we observed a similar transient pattern within 1.8–2.25 eV to that observed in the 580-nm pumping case. This is understandable because the population in thus excited S_2 state will undergo rapid internal conversion (IC) to the S_1 state (due to the well-known Kasha’s rule) and, consequently, what the WLC probes is the pure singlet-space dynamics including GSB (ground-state bleaching), ESA (excited-state absorption), and SE (stimulated emission), as annotated in the upper left panel. It should be noted that we did not observe any SET pattern corresponding to the $T_3 \rightarrow T_2$ transition (within 1.2–1.8 eV). These observations indicate that in the conventional pump–probe scheme the rapid IC ($S_2 \rightarrow S_1$) process prevails over the much less competitive ISC ($S_2 \rightarrow T_3$) process, which in turn highlights the advantage of the fs-TRPP technique in disclosing the triplet dynamics, as we proposed in the Introduction Section [*"to increase the ISC probability by applying an ultrafast broadband white-light continuum (WLC) as the excitation light source to populate vibrational manifolds in a certain excited singlet state. As the ISC efficiency can be enhanced by certain excited vibrational modes, the use of broadband WLC that facilitates the excitation of different vibrational modes is expected to favor ISC and hence enhance population transfer from the excited singlet state to the nearby excited triplet state."*]. **Lower left panel:** The ME pattern recorded with a 580-nm "pump" in the fs-TRPP regime (adapted from Fig. 5a of Article). **Lower right panel:** The ME pattern recorded with a 400-nm "pump" in the fs-TRPP regime. The same WLC "probe" (real excitation source) was used. **Relevant discussions:** In the fs-TRPP scheme (using the weak WLC "probe" to excite S_2, and subsequently the strong, "quasi-monochromatic" 400-nm "pump" to modulate the T_3 population), we also observed the ME pattern within 1.2–1.8 eV like the experiment with the 580-nm pump. As we have stated in the main text of Article (refer to the end of Section 5), this observation conforms well to the fact that triplet states lying above T_3 (labeled $T_{n(n>3)}$ in Fig. 3 of Article) abound, thus making the modulating "pump" laser with different central wavelengths readily find a way out for resonantly driving vibronic transitions from T_3 to these higher-lying triplet states. Such insensitivity to the "pump" wavelengths in the fs-TRPP regime validates its role as a population modulator. It is worth noting that the observation of weaker transient pattern in the 400-nm case than that in the 580-nm case arises most likely as a result of different transition strengths from the T_3 state to different upper triplet states coupled by the "quasi-monochromatic" modulating lasers applied (central wavelength at 400 or 580 nm).

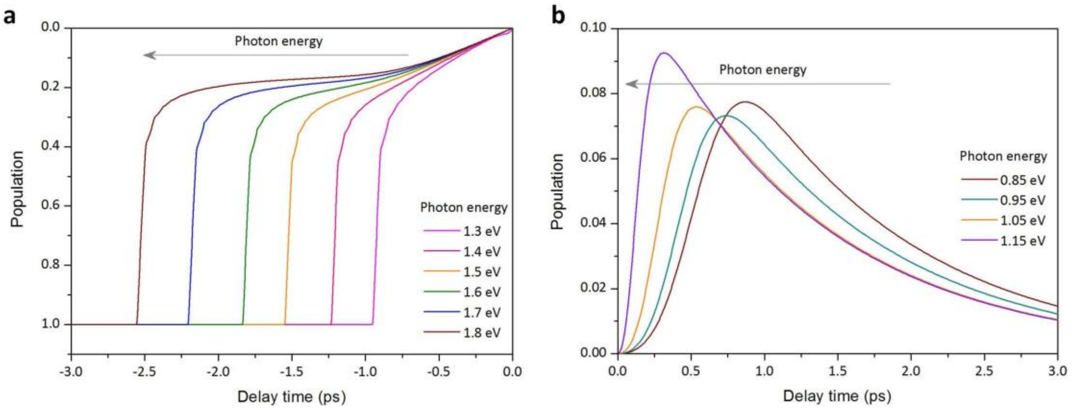

Fig. S5 Simulated temporal evolution of the vibrational populations associated with the ME ($T_3 \rightarrow T_2$) and SET ($T_2 \rightarrow T_1$) kinetics observed in MG. (a) Representative simulation results for the T_3 manifolds (for ME) at different probe photon energies (from 1.3 to 1.8 eV with 0.1-eV steps). The population of the T_3 state is depicted on the y axis. This set of population evolution profiles simulates only the initial, population built-up (till saturation) stage of our observed avalanche-like kinetics of ME ($T_3 \rightarrow T_2$) as shown in Fig. 5b of Article. (b) Representative simulation results for the T_2 manifolds (for SET) at different probe photon energies (from 0.85 to 1.15 eV with 0.1-eV steps). The population of the T_2 state is depicted on the y axis. Note here that an identical set of time constants—1.2, 10, and 0.05 ps for ISC, IC, and IVR, respectively—was used for both cases. Adjusting the time parameters to these fixed time constants was based on the numerical simulations under a crude model (see the following Appendix) that attempts to accommodate both the ME ($T_3 \rightarrow T_2$) and the SET ($T_2 \rightarrow T_1$) behaviors as close as possible to the experimental observations. Undoubtedly, such modeling and simulations are rather crude, and a more accurate description from the theoretical perspective evokes a more rigorous yet sophisticated modeling framework that takes account of the currently neglected, intractable factors as much as possible. ME, SET, ISC, IC, IVR, and MG are the acronyms for modulated emission, stimulated emission between triplets, intersystem crossing, internal conversion, intramolecular vibrational redistribution, and malachite green, respectively.

Appendix to Fig. S5: A crude model describing the ME ($T_3 \rightarrow T_2$)

The $T_3 \rightarrow T_2$ ME signals (S_{ME}) observed under the fs-TRPP regime can be described by

$$S_{\mathrm{ME}} \propto -\left|\mu^{T_3 \rightarrow T_2}\right|^2 \cdot \mathrm{FC}(i,j) \cdot n_i^{T_3} \cdot (1-n_j^{T_2}), \tag{S1}$$

where $\mu^{T_3 \rightarrow T_2}$ denotes the $T_3 \rightarrow T_2$ transition dipole moment, $\mathrm{FC}(i,j)$ the Franck–Condon factor accounting for the wavefunction overlap of the i-th and j-th vibrational levels, and $n_i^{T_3}$ ($n_j^{T_2}$) the population in the i-th (j-th) vibrational level of the T_3 (T_2) state. The temporal evolutions of $n_i^{T_3}$ rely on the populations in its adjacent, iso-energetic vibrational levels of the S_2 state, denoted $n_k^{S_2}$, and can be expressed as

$$\frac{\partial n_i^{T_3}}{\partial t} = \left.\frac{n_k^{S_2}}{\tau_{\mathrm{ISC}}}\right|_{E_i^{T_3}=E_k^{S_2}} - \frac{n_i^{T_3}}{\tau_{\mathrm{IC}}} + \sum_{l>i} \frac{n_l^{T_3}}{\tau_{\mathrm{IVR}}^{l,i}} - \sum_{i>h} \frac{n_i^{T_3}}{\tau_{\mathrm{IVR}}^{i,h}} - \frac{n_i^{T_3}}{\tau_{\mathrm{ME}}}, \tag{S2}$$

Note here that an identical set of time constants τ_{ISC}, τ_{IC}, and τ_{ME} was taken in our simulations for describing the involved intersystem crossing (ISC), internal conversion (IC), and modulated emission (ME) processes, based on the assumption that the intramolecular processes of the same type could bear similar intrinsic decay rates in this singlet–triplet coupled system.

Special care must be taken in the much faster intramolecular vibrational redistribution (IVR) processes. For instance, $\tau_{\mathrm{IVR}}^{l,i}\,(l>i)$ describes an IVR process cascading from the upper l-th to the lower i-th vibrational levels within a certain singlet or triplet state. Generally speaking, larger vibrational level separations (i.e., larger $l-i$ values) correspond to slower IVR processes (i.e., larger $\tau_{\mathrm{IVR}}^{l,i}\,(l>i)$ values). To take this into account, we assume that $\tau_{\mathrm{IVR}}^{l,i}$ takes the following explicit form

$$\tau_{\mathrm{IVR}}^{l,i} = (l-i)^2 \tau_{\mathrm{IVR}}, \tag{S3}$$

where a common τ_{IVR} constant is used to account for any IVR ($l-i=1$) processes. The rational assumption of Equation S3 allows us to establish a set of IVR cascade rate equations *of an analytic form* to describe the population evolutions within an excited state *e* with *m* (in total) vibrational levels:

$$\begin{aligned}
\frac{\partial n_m^e}{\partial t} &= -\frac{1}{\tau_{\mathrm{IVR}}} n_m^e \left(1+\frac{1}{2^2}+\frac{1}{3^2}+\cdots+\frac{1}{(m-1)^2}\right) = -\frac{\pi^2}{6\tau_{\mathrm{IVR}}} n_m^e,\\
\frac{\partial n_{m-1}^e}{\partial t} &= \frac{1}{\tau_{\mathrm{IVR}}} n_m^e - \frac{\pi^2}{6\tau_{\mathrm{IVR}}} n_{m-1}^e,\\
\frac{\partial n_{m-2}^e}{\partial t} &= \frac{1}{2^2\tau_{\mathrm{IVR}}} n_m^e + \frac{1}{\tau_{\mathrm{IVR}}} n_{m-1}^e - \frac{\pi^2}{6\tau_{\mathrm{IVR}}} n_{m-2}^e,\\
&\vdots\\
\frac{\partial n_{m-k}^e}{\partial t} &= \sum_{j=1}^{k} \frac{1}{j^2\tau_{\mathrm{IVR}}} n_{m-k+j}^e - \frac{\pi^2}{6\tau_{\mathrm{IVR}}} n_{m-k}^e.
\end{aligned} \tag{S4}$$

Solving Equation S4 yields

$$\begin{aligned}
n_m^e &= \exp\left(-\frac{\pi^2}{6\tau_{\mathrm{IVR}}} t\right),\\
n_{m-1}^e &= \frac{t}{\tau_{\mathrm{IVR}}} \exp\left(-\frac{\pi^2}{6\tau_{\mathrm{IVR}}} t\right),\\
n_{m-2}^e &= \left[\frac{t}{2^2\tau_{\mathrm{IVR}}} + \frac{t^2}{2!\tau_{\mathrm{IVR}}^2}\right] \exp\left(-\frac{\pi^2}{6\tau_{\mathrm{IVR}}} t\right),\\
n_{m-3}^e &= \left[\frac{t}{3^2\tau_{\mathrm{IVR}}} + \frac{t^2}{2^2\tau_{\mathrm{IVR}}^2} + \frac{t^3}{3!\tau_{\mathrm{IVR}}^3}\right] \exp\left(-\frac{\pi^2}{6\tau_{\mathrm{IVR}}} t\right),\\
&\vdots
\end{aligned}$$

$$
\begin{aligned}
n_k^e &= \exp\left(-\frac{\pi^2}{6\tau_{\mathrm{IVR}}}t\right)\sum_{j=1}^{m-k} a_j \frac{t^j}{\tau_{\mathrm{IVR}}^j} \\
&\approx \exp\left(-\frac{\pi^2}{6\tau_{\mathrm{IVR}}}t\right)\exp\left(\frac{c_k}{\tau_{\mathrm{IVR}}}t\right) = \exp\left(\frac{c_k'}{\tau_{\mathrm{IVR}}}t\right).
\end{aligned}
\tag{S5}
$$

It is seen from Equation S5 that the population in a certain *k*-th vibrational level, n_k^e, could evolve temporally in an exponential growing fashion if the c_k' constant takes a positive value, which is most likely the case for the MG molecule under investigation as it seems hard to accommodate the initial, exponential build-up behavior in the observed ME kinetics (Fig. 5b of Article) otherwise. Note that we adopted a set of similar modeling and simulation procedures (e.g., with similar forms of Equations S1 and S2 but with different annotations for the involved states; not given here) to describe the SET ($T_2 \rightarrow T_1$) behavior (*cf*. the resulting Fig. S5b *vs*. Fig. 8b of Article).